Received: 20 July 2020 | Revised: 3 August 2021 | Accepted: 13 November 2021

DOI: 10.1002/jbm.b.34970

RESEARCH ARTICLE

Society For Biomaterials | WILEY

Mechanical in vitro fatigue testing of implant materials and components using advanced characterization techniques

Nils Wegner | Martin Klein | Ronja Scholz | Daniel Kotzem | Marina Macias Barrientos | Frank Walther

Chair of Materials Test Engineering (WPT), TU Dortmund University, Dortmund, Germany

Correspondence
Nils Wegner and Frank Walther, Chair of Materials Test Engineering (WPT), TU Dortmund University, Baroper Str. 303, D-44227, Dortmund, Germany
Email: nils.wegner@tu-dortmund.de and frank.walther@tu-dortmund.de

Funding information
Deutsche Forschungsgemeinschaft, Grant/Award Number: 394479422

[Correction added on 4 March 2022, after first online publication: Copyright statement has been updated.]

Abstract

Implants of different material classes have been used for the reconstruction of damaged hard and soft tissue for decades. The aim is to increase and subsequently maintain the patient's quality of life through implantation. In service, most implants are subjected to cyclic loading, which must be taken particularly into consideration, since the fatigue strength is far below the yield and tensile strength. Inaccurate estimation of the structural strength of implants due to the consideration of yield or tensile strength leads to a miscalculation of the implant's fatigue strength and lifetime, and therefore, to its unexpected early fatigue failure. Thus, fatigue failure of an implant based on overestimated performance capability represents acute danger to human health. The determination of fatigue strength by corresponding tests investigating various stress amplitudes is time-consuming and cost-intensive. This study summarizes four investigation series on the fatigue behavior of different implant materials and components, following a standard and an in vitro short-time testing procedure, which evaluates the material reaction in one enhanced test set-up. The test set-up and the applied characterization methods were adapted to the respective application of the implant with the aim to simulate the surrounding of the human body with laboratory in vitro tests only. It could be shown that by using the short-time testing method the number of tests required to determine the fatigue strength can be drastically reduced. In future, therefore it will be possible to exclude unsuitable implant materials or components before further clinical investigations by using a time-efficient and application-oriented testing method.

KEYWORDS
fatigue assessment, in vitro short-time testing method, magnesium implants and stents, titanium abutments, ultra-high molecular weight polyethylene

1 | INTRODUCTION

In various surgical disciplines, the replacement of lost hard tissue after trauma, tumors, or malformations or to restore/support body functions are performed with permanent or bioresorbable implants.[1] Permanent implants are often made of biocompatible titanium alloys, such as Ti-6Al-4V.[2] Bioresorbable implants, which make second surgeries to remove permanent fracture and reconstruction plates obsolete, are made of magnesium alloys.[3] For the safe use of implants, the mechanical and corrosive property profile (including fatigue and degradation behavior) must be characterized so that premature mechanical failure is prevented and the risk to human health is reduced. Several reports demonstrate that material fatigue is responsible for a large proportion of failing implants[4,5] and that

accurate prediction of the lifetime of mechanically loaded implants is a challenge for medical engineering.[6] Examining the performance in vivo is hardly reproducible to be transferred to the human body. Existing in vitro testing procedures are time-consuming and cost-intensive, so that quick approval of medical products is not possible. Due to the different fields of application and the associated requirement profiles, application-oriented testing also differs. In the following, current in vitro testing procedures are presented and explained on the example of four different implant materials to underline the need for an adaptable short-time testing method. Thereby, the considered load collective shall become increasingly complex. Hence, the two permanent materials/structures ultra-high molecular weight polyethylene (UHMWPE), and titanium abutments are discussed first. The corrosion influence plays a minor role here, but the degree of complexity increases due to the abutment geometry. Subsequently, magnesium and further magnesium stents are presented, whereby degradation has a significant influence on the mechanical properties.

1.1 | UHMWPE implants

Due to a broad property profile of mechanical, chemical, and physical properties as well as in vivo verified biocompatibility,[7–9] UHMWPE has been used for decades as a material in prostheses, for example in hip, knee or shoulder joints.[10,11] For the established applications, mainly frictional loads are present. More recent approaches are evaluating its use as a bone replacement material for large bone defects. For this application, the difference in stress type has to be considered.[7,12] Due to changing damage mechanisms and the usually much lower fatigue strength compared to quasistatic strength of a material, these investigations are essential. Due to the established, wear-dominated application in prostheses, many studies focus on tribological investigations.[13–16] For cyclic loading, fatigue crack initiation and propagation and the influence of the microstructure (e.g., crosslinking) are intensively investigated.[17] For crack propagation, notched specimens are loaded at a stress ratio of $R = 0.1$.[18,19,22] Investigations with the aim of fatigue life evaluation based on an S–N curve, as addressed in this article, hardly exist. The few existing investigations can be divided into uniaxial[20–22] and multiaxial[23,24] loading. Urriés et al. investigated the effect of different irradiation treatments on the fatigue strength of UHMWPE. The tests were performed with a sinusoidal stress-time function at a stress ratio of $R = 0$ and a frequency of $f = 1$ Hz. A fatigue strength of approximately 20 MPa was determined for a failure criterion of a total strain of 12%.[22] A similar experimental approach was used by Medel et al. to characterize different irradiation doses and a thermal post-treatment.[21] Sobieraj et al. used pre-aging as well as testing of specimens in phosphate-buffered saline at body temperature. The tests were performed on notched specimens at a stress ratio of $R = 0.04$–0.05 at a frequency of $f = 2$ Hz. Through the tests, the fatigue strength was estimated between $\sigma_a = 10.17$ MPa and $\sigma_a = 11.35$ MPa.[20]

1.2 | Titanium abutments

Abutments are the connecting element between the dental implant and the visible dental crown, thus they transmit the forces from the oral cavity, which arise, for example, during chewing, and are, therefore, exposed to daily multiaxial stress.[25] Due to its high corrosion resistance and biocompatibility in combination with a high strength-to-weight ratio,[26–28] titanium alloys, among others, are state of the art for this application.[29] Concerning mechanical testing, the standard DIN EN ISO 14801 regulates the fatigue testing of endosseous dental implants. It is specified that a constant amplitude test (CAT) should start with a load corresponding to 80% of the quasistatic strength and thereafter be gradually reduced resulting in a time-consuming testing procedure. Generally, many studies use the experimental set-up and procedure from this standard, yet there is a significant inconsistency between many studies in terms of the forces applied, the frequency used, and the environmental conditions.[30] The research objectives also differ: for example, the influence of fatigue loading on the micro-gap[31] or micromotion[32] between implant and abutment or the reverse torque value[33] is often investigated. Most studies do not vary the applied force but the number of cycles[31] or the influence of the preload torque.[32] Studies investigating several loads define the levels based on the quasistatic strength (as described in the standard)[34] so that the procedure is not based on previously obtained knowledge. In contrast, Foong et al. investigated the approach of a short-term testing method in the form of a "stepped fatigue loading protocol." The tests were force-controlled with an initial load of 50 N and a load increase of 50 N up to 400 N. Sample failure was detected by an abrupt increase of the displacement or a force decrease. During the tests, the samples were moistened by a gauze soaked in saline solution. Evaluation of in situ measured values was not performed.[35] Another short-term method "step-stress accelerated life test" is described by Freitas-Júnior et al. Here, a cyclic load is applied at 30% of the quasistatic strength and gradually increased to 60%. Damage accumulation and fractographic analyses are used to determine a failure probability as a function of load level and number of cycles.[36]

1.3 | Magnesium implants and stents

Bioresorbable magnesium implants are regarded as promising biomaterials of the future in surgically oriented fields of medicine.[3] In addition to stents and screws, the development of degradable fracture and reconstruction plates is the focus of efforts.[37,38] Due to the low corrosion resistance, magnesium dissolves in the aqueous environment of the human body, so that a second surgery for removal is not necessary. The intense and partial non-uniform corrosion behavior with release of hydrogen gas of magnesium alloys in a physiological environment proves to be a challenge in clinical use.[39,40] In this context, the decrease in cross-sectional area and the formation of corrosion scars lead to a significant decrease in mechanical stability.[6,41,42] Despite these limitations, only a few studies exist on the corrosion

fatigue behavior of biomedical magnesium systems. The existing studies can be divided into uniaxial and multiaxial cyclic loading. Multiaxial loading includes rotating bending[43] and three- or four-point bending tests.[44] Due to the loading type in this article, the focus will be on uniaxial loading studies. The majority of these studies use a stress ratio of $R = -1$, a frequency of $f = 10$ Hz, and a maximum number of cycles between $N_f = 5 \times 10^5$ and 10^7.[45–47] To determine the corrosion fatigue strength, CAT are performed at different stress levels until N_f is reached.[45,47–49] Superimposing with corrosive load results in a significant decrease in fatigue properties. The studies attribute this to different damage mechanisms: Bias et al. relate this to stress concentrations and thus favored corrosive attack between the different phases,[45] Gu et al. attribute this to extrusions and intrusions, which are preferentially corrosively attacked.[46] Han et al. describe damage to the corrosion layer under cyclic loading, resulting in corrosion scars at the damaged areas.[50] Other studies mention hydrogen embrittlement at the crack tip and thus accelerated crack propagation. A common feature between all studies is the occurrence of localized corrosion effects, which promote crack initiation and lead to premature failure.[49,51]

Due to their individual geometry, magnesium stents are described in a separate section, although the general statements about magnesium remain valid. Stents are often used in angioplasty surgeries for artery and, less frequently, vein support and to avoid early arterial recoil.[52] Permanent stents increase the risk of long-term complications such as stent restenosis.[53] To determine and evaluate the mechanical properties of bioresorbable magnesium stents, mainly quasistatic tensile tests with[54] or without pre-corrosion are performed. These results are often used to validate finite element simulation.[55,56] Few studies exist on the experimental determination of corrosion fatigue properties, whereas recent studies address the simulation of these properties.[57,58] Other studies use a simplified approach and examine wires in strain- or displacement-controlled bending[59] or rotating-bending tests.[60] Analogous to the damage mechanisms described previously, the decrease in fatigue properties was accompanied by the formation of localized corrosion.

It can be concluded that there are no or hardly any studies on fatigue behavior for the different implant materials. Testing under application-oriented in vitro conditions is even less frequently considered. A systematic in vitro short-term test method with in situ detection and subsequent evaluation of the material reaction for implant materials is not known to the authors. Therefore, this review article presents the application and verification of such a method on the example of bioresorbable magnesium as well as permanent UHMWPE and titanium implants, which could be transferred to various other implant materials in the future.

2 | MATERIALS AND METHODS

The general experimental set-up of the corrosion fatigue tests is similar and is adaptable to the respective loading case (Figure 1A). A simulated body fluid (SBF) is temperature-controlled by an external heat source and pumped via a peristaltic pump to the corrosion cell. The clamping of the specimen or compression dies for force transmission is adapted to the respective application (Figure 1B–E). As monitoring, the control unit of the testing system records measurement data during the tests. Further information on the experimental set-ups is given in the respective subchapters.

2.1 | Magnesium implants

The magnesium alloy WE43 (yttrium, rare earth [RE]) was produced via the process route of laser powder bed fusion using three different

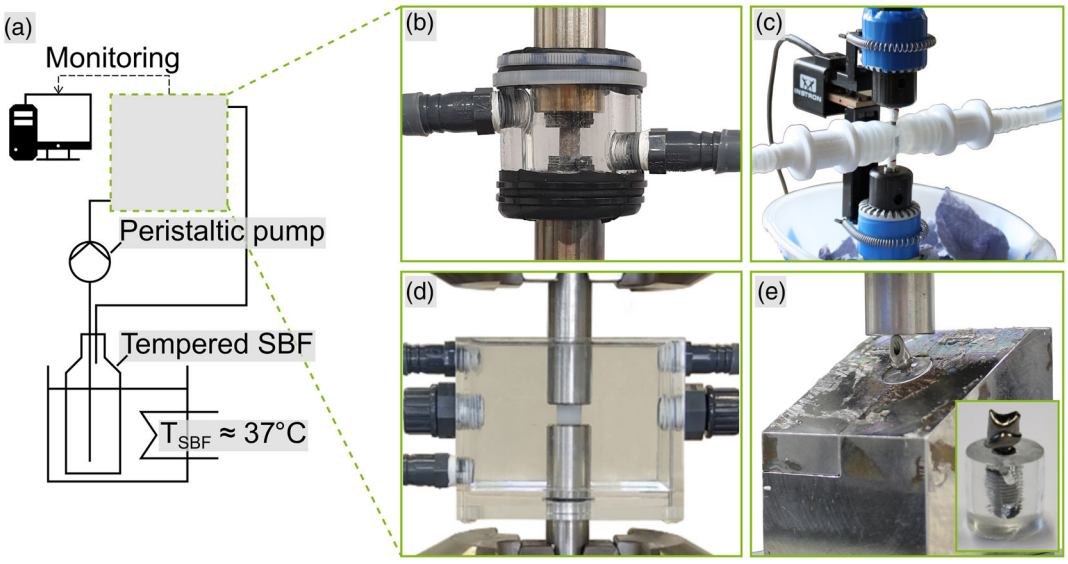

FIGURE 1 (A) General experimental set-up for in vitro experiments with: (B) additively manufactured magnesium (standard geometry); (C) magnesium stents; (D) UHMWPE (standard geometry); (E) titanium abutments. UHMWPE, ultra-high molecular weight polyethylene

TABLE 1 Parameter sets for L-PBF process

Batch	d_H (µm)	v_s (mm/s)	t (µm)	Exposure	Grain size (µm)[a]
A	15	1000	50	Single	1.74
B	110	300	30	Single	1.44
C	100	450	50	Double	1.44

[a]Measured with a scanning electron microscope (SEM, Mira 3 XMU, Tescan, Dortmund, Germany).
Abbreviation: L-PBF, laser powder bed fusion.

parameter sets (Table 1). Constant laser power was applied $P_L = 100$ W, whereas the hatch distance d_H, scanning speed v_S, layer thickness t, and exposure were varied. As specimen geometry, cylinders according to the German standard DIN 50106 (diameter $d_0 = 7$ mm, height $h_0 = 10.5$ mm) were chosen, for fatigue tests, the front surfaces were polished plane-parallel to 5.5 µm. For corrosion tests, the samples were cold-embedded and polished with water-free diamond suspension up to 1 µm.

The macrostructure of the initial condition (i.c.) was determined by µ-computed tomography (µCT, XT H 160, Nikon Metrology NV, Leuven, Belgium). Immersion tests were carried out on the embedded samples using a SBF at 37°C according to Kokubo[61] in a double-walled corrosion cell with detection of the hydrogen volume produced. Based on these results, two batches were selected for the (corrosion) fatigue tests. CAT were performed with a stress ratio of $R = 10$ (compression-compression loading), a sinusoidal stress-time function, a test frequency of $f = 10$ Hz in SBF at 37°C and as a reference in air at room temperature (RT, 21 ± 0.5°C) using a servo-hydraulic testing system ($F_{max} = \pm 45$ kN, Schenck PC 63 M, Instron, Norwood, USA), which is equipped with an Instron 8800 controller. Inconel compression dies with tungsten carbide cobalt plates were used to apply the load, and a corrosion cell with a thermostat as well as a peristaltic pump was used to simulate the physiological conditions (Figure 1A,B). Fatigue tests were carried out until failure or stopped after a maximum number of cycles of $N_{limit} = 2{\cdot}10^6$.

2.2 | Magnesium stents

The magnesium alloy WE43 was also used for the stents with an inner diameter of $d_i = 1.4$ mm and an outer diameter of $d_o = 1.8$ mm. These values were used to calculate the stress, assuming a hollow cylinder. CAT were carried out at different stress levels with a sinusoidal stress-time function at a stress ratio of $R = 0.1$ (tension-tension loading) and a frequency of $f = 20$ Hz. The stents were clamped via an adapted clamping chuck (Figure 1C and Figure 4A) in a magnetic micro testing system ($F_{max} = \pm 500$ N, MMT-500NV-10, Shimadzu, Duisburg, Germany). Analogous to Section 2.1, the experiments were performed in a SBF at 37°C[61] and as a reference in air at RT. The fluid was tempered using a heating plate with an internal control circuit and circulated through the stent by a peristaltic pump. The maximum number of cycles was set to $N_{limit} = 10^7$.

2.3 | Titanium abutments

The abutments were manufactured from titanium Grades 4 and 5 in the form of a cheek and anterior tooth. The experimental set-up was based on the German standard DIN EN ISO 14801. The threads were embedded in a polymer mass and fixed in a two-part device (Figure 1A,E), so that the compression loading was applied through a compression die under an angle of 30° ± 2° by a servo-hydraulic testing machine ($F_{max} = \pm 20$ kN, EHF-LV20, Shimadzu, Duisburg, Germany). Fatigue tests were performed at RT (21 ± 0.5°C) in a minimum essential medium and in air for reference. For all fatigue tests, a sinusoidal load-time function at a load ratio of $R = 10$ (compression-compression loading) and a frequency of $f = 5$ Hz was used. The multiple amplitude tests (MAT) started at a force of $F_{max,start} = 0.4$ kN that was increased by $\Delta F_{max} = 0.2$ kN every $\Delta N = 10^3$ cycles. Based on the MAT results, load levels for CAT were selected. For CAT, a maximum number of cycles $N_{limit} = 2 \times 10^6$ was used.

2.4 | UHMWPE implants

The UHMWPE bulk material (Mass average molar mass of $M_w = 5 \times 10^6$ g/mol, PJSC "Kazanorgsintez," Kazan, Russia) was produced by thermopressing at a temperature of 180°C and a pressure of 70 MPa (according to Reference 7), from which rectangular prisms ($10 \times 4 \times 10$ mm^3) were milled in accordance with DIN EN ISO 604. In order to reduce deviations in subsequent tests, the side surfaces were grounded to an average surface roughness of $Ra < 0.3$ µm.

Fatigue tests were performed on a servo-hydraulic testing system ($F_{max} = \pm 25$ kN, $M_{max} = \pm 200$ Nm, Bionix 858, MTS, Berlin, Germany) with a stress ratio of $R = 10$ (compression-compression loading), a sinusoidal stress-time function, and a frequency of $f = 5$ Hz. For MAT, the initial stress was set to $\sigma_{max,start} = 7.5$ MPa and was increased by $\Delta\sigma_{max} = 2.5$ MPa every $\Delta N = 10^4$ cycles. During the tests, nominal stress–strain hystereses (sampling frequency $f_S = 1000$ Hz) were recorded, on which basis different characteristic values were evaluated to determine the stress levels for CAT. Tests were executed in two different environments, to simulate physiological conditions a SBF according to Kokubo et al.[61] at a temperature of 37°C and as a reference air at RT (21 ± 0.5°C). Compression dies were used to apply the load, and a corrosion cell with a thermostat as well as a peristaltic pump was used to simulate the physiological conditions (Figure 1D and Figure 7A). A maximum number of cycles of $N_{limit} = 2 \times 10^6$ cycles was defined as a run-out for CAT. A nominal compressive strain of $\varepsilon_{c,max} = 20\%$ was used as failure criterion based on previously performed quasistatic compression tests. Both, in the i.c. and after mechanical loading, the samples were examined utilizing hardness measurements and infrared spectroscopy.

To determine the micromechanical properties, hardness measurements with an indentation depth of $h = 10$ µm were carried out on a dynamic ultra-micro-hardness testing system (DUH 211, Shimadzu, Duisburg, Germany). For each sample and condition, three measurements were performed, averaged and the change in Martens hardness

ΔHM_{CAT} after mechanical loading was calculated in relation to the initial value HM_0. The chemical composition was investigated by Fourier-transform infrared (FTIR) spectroscopy (IRTracer-100, Shimadzu, Duisburg, Germany) equipped with an ATR module (attenuated total reflectance, Germanium). The wavenumber $\bar{\nu}$ interval from 3600 to 400 cm^{-1} was characterized by 20 scans per sample and a resolution of 2 cm^{-1}. The spectra were evaluated using the corresponding software LabSolutionsIR and afterward normalized via Origin 2018, so that experimental configurations between sample and equipment can be minimized.

3 | RESULTS

3.1 | Magnesium implants

In the following, selected experimental results regarding the cyclic deformation behavior of the additively manufactured magnesium alloy WE43 are highlighted to demonstrate the reliability of the in vitro short-time testing method proposed. The complete experimental results were published in References 62,63.

The results of the macroscopic structural investigations using µ-computed tomography (µCT) are shown in Figure 2 with the pore density and sphericity S plotted over the equivalent pore diameter d_p. The sample volumes analyzed range from 318 mm^3 (Batch A) to 335 mm^3 (Batch B). Evaluation of the results shows that the pore distribution, as well as the size and shape, vary with changing process parameters. Batch B reaches the maximum relative density >99.9%, whereas A and C reach relative densities >99.5%. According to the relative density, the pore densities for Batch A and C are at a higher level than for Batch B (Figure 2A). To evaluate the influence of the pore shape, the sphericity S as a function of the equivalent pore diameter d_p is also considered (Figure 2B). The sphericity decreases with increasing d_p, with Batch A and C reaching higher peak values with $S < 0.3$ for $d_p = 1000$ µm, whereas no pores with $d_p > 325$ µm or $S < 0.3$ could be detected for Batch B.

Figure 3A summarizes the results of the immersion tests. For all three batches, the specific hydrogen volume $V_{H_2,spec}$ shows a similar qualitative course over the immersion time t. The corrosion rates are determined from the linear slope of the regression curves and are $\dot{m}_{corr} = 7.2 \times 10^3$ mg/(cm^2 a) for Batch A, 2.2×10^3 mg/(cm^2 a) for Batch B, and 3.1×10^3 mg/(cm^2 a) for Batch C.

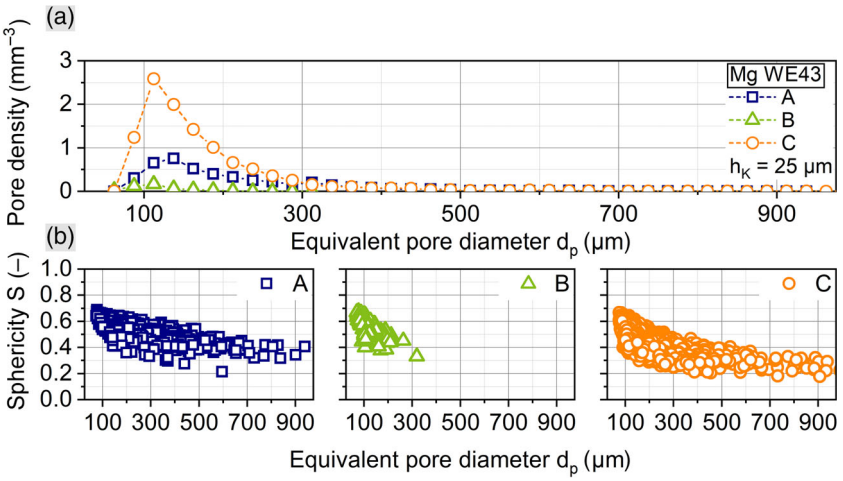

FIGURE 2 µCT results of (A) pore density and (B) sphericity S as a function of the equivalent pore diameter d_p[63]

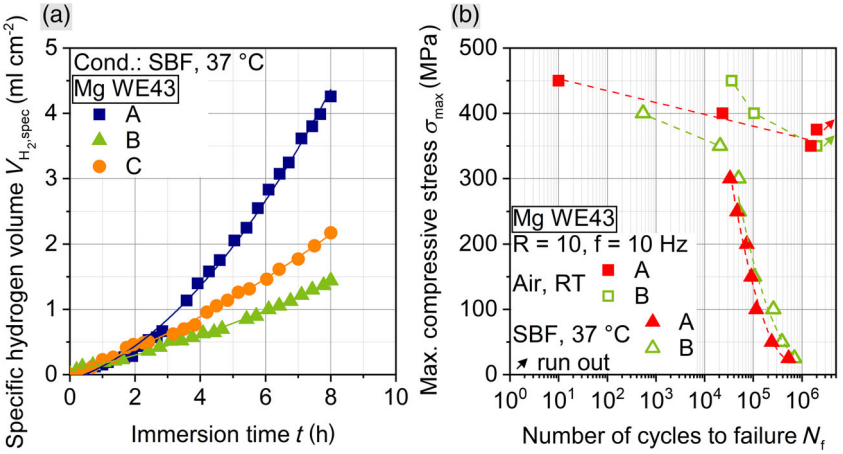

FIGURE 3 Results of (A) immersion tests of Batches A, B, C and (B) trend S–N curves for Batches A and B in air (RT) and in SBF at 37°C[62]

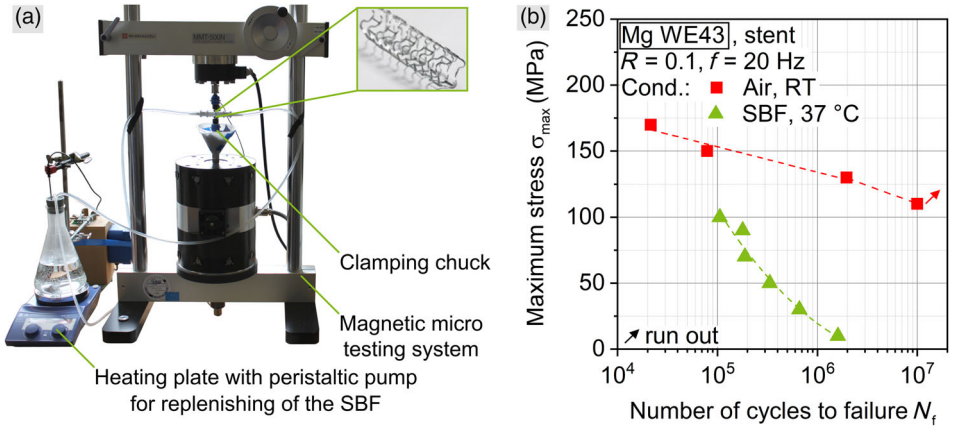

FIGURE 4 (A) Experimental set-up for in vitro experiments with magnesium stents; (B) trend S–N curves for magnesium (WE43) stents in air and in SBF at 37°C

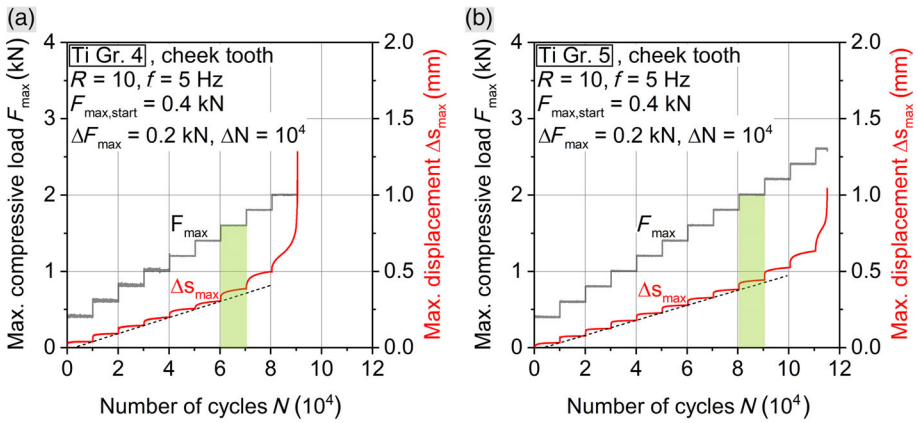

FIGURE 5 Exemplary results of multiple amplitude tests with visualization of fatigue strength estimation for (A) titanium Grade 4 cheek tooth and (B) titanium Grade 5 cheek tooth

The results of the subsequent fatigue investigations (Batch A and B) are summarized in Figure 3B with the maximum compressive stress σ_{max} plotted over the number of cycles to failure N_f. Particularly in the low cycle fatigue (LCF) range, the tests in air show clear differences between the two batches. For $\sigma_{max} = 450$ MPa ($N_{f,B,RT} = 35{,}979$ and $N_{f,A,RT} = 10$) and 400 MPa ($N_{f,B,RT} = 102{,}848$ and $N_{f,A,RT} = 23{,}192$), Batch B achieves a higher number of cycles to failure. In contrast, the differences in the high cycle fatigue (HCF) range are smaller, with run-outs being achieved at $\sigma_{max} = 350$ MPa (Batch B) and 375 MPa (Batch A), with Batch A achieving $N_{f,A,RT} = 1{,}522{,}777$ for a further maximum compressive stress of $\sigma_{max} = 350$ MPa.

The tests in the SBF show a drastic decrease in fatigue properties for both batches. Compared to the tests in air, there is already a decrease in the number of cycles to failure in the LCF range. In the transition to the HCF range, the slope of both curves changes to much lower number of cycles to failure. At the lowest σ_{max} (= 25 MPa) tested, number of cycles to failure of $N_{f,A,SBF} = 527{,}390$ and $N_{f,B,SBF} = 691{,}729$ are achieved, which are below the maximum number of cycles $N_{limit} = 2 \times 10^6$ defined previously.

3.2 | Magnesium stents

The results of CAT are summarized in Figure 4B with the maximum stress σ_{max} plotted in semi-logarithmic application over the number of cycles to failure N_f. The data points of the tests in air lie approximately on a straight line in the semi-logarithmic plot. For $\sigma_{max} = 110$ MPa, a run-out is achieved at $N_{limit} = 10^7$. The qualitative course of the tests in the SBF is similar to the results of the additively manufactured magnesium specimens in Section 3.1. The lowest tested maximum stress is $\sigma_{max} = 10$ MPa, for which a number of cycles to failure $N_{f,SBF} = 1{,}599{,}775$ is achieved, which is far below $N_{limit} = 10^7$.

3.3 | Titanium abutments

Figure 5 shows two exemplary results of MAT for titanium cheek tooth Grade 4 (A) and Grade 5 (B). The maximum compressive load F_{max} is plotted as the controlled value and the maximum displacement Δs_{max} as the measured value over the number of cycles N. The qualitative course of Δs_{max} is similar for both materials and increases gradually with increasing load, whereas it takes on a degressive course within one load step (F_{max} = const.). The differences appear through a higher displacement for Grade 4 at the same loads and through failure at a higher maximum load F_{max} for Grade 5 ($F_{max,f,Gr4} = 2$ kN and $F_{max,f,Gr5} = 2.6$ kN). Failure for both materials is characterized by a sudden increase in Δs_{max}.

Figure 6 summarizes the results of the CAT in the form of trend S–N curves for titanium anterior (A) and cheek tooth (B). In a semi-logarithmic plot, the maximum compressive load F_{max} is plotted over the number of cycles to failure N_f, with run-outs marked by an arrow in the respective color. Within a tooth geometry, differences between

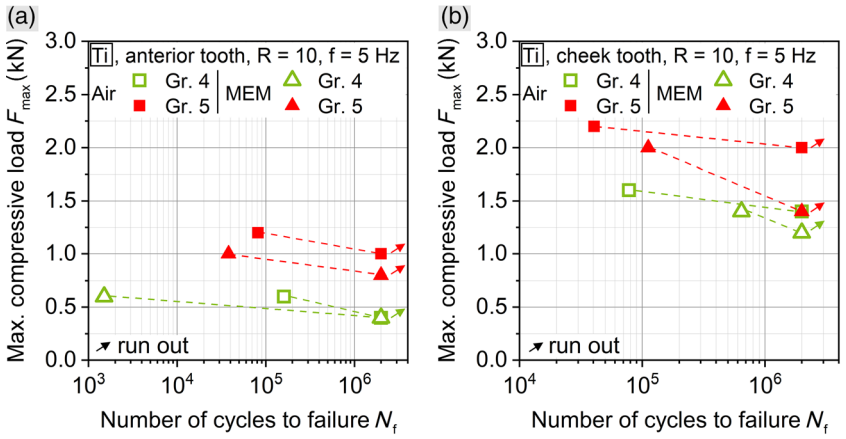

FIGURE 6 Trend S–N curves in air and in a minimum essential medium for (A) titanium anterior tooth and (B) titanium cheek tooth

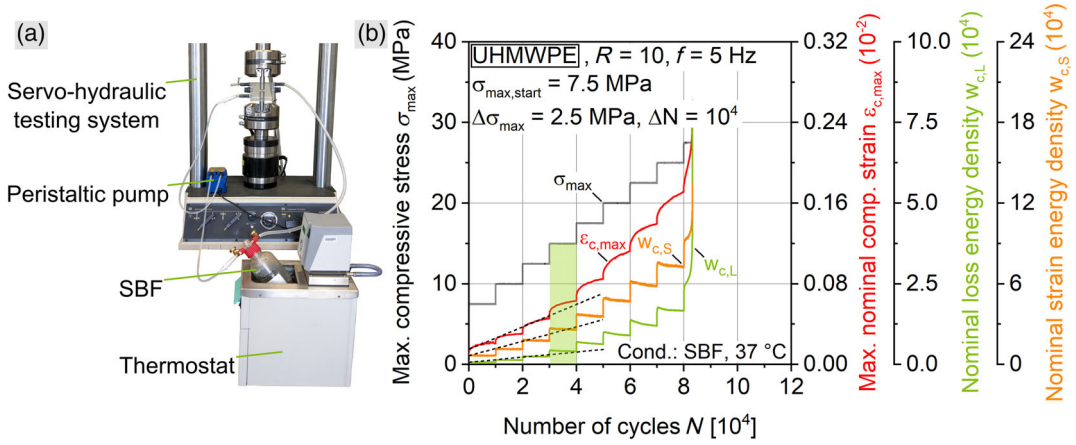

FIGURE 7 (A) Experimental set-up for in vitro experiments with UHMWPE;[64] (B) exemplary result of a multiple amplitude test on UHMWPE in a simulated body fluid at 37°C.[65] UHMWPE, ultra-high molecular weight polyethylene

Grade 4 and 5 as well as between the test conditions are observable. For the anterior tooth, higher fatigue strengths for Grade 5 $F_{max,fs,Gr5,RT} = 1$ kN ($F_{max,fs,Gr4,RT} = 0.8$ kN) as well as for the tests in air ($F_{max,fs,SBF} = 0.4$ kN, for both alloys) are shown. The fatigue strengths for the different environmental conditions of $F_{max,fs,Gr5,RT} = 2$ kN and $F_{max,fs,Gr5,SBF} = 1.4$ kN for Grade 5 and of $F_{max,fs,Gr4,RT} = 1.4$ kN and $F_{max,fs,Gr4,SBF} = 1.2$ kN for Grade 4 are shown in this diagram.

3.4 | UHMWPE implants

In the following, selected experimental results regarding the fatigue behavior of UHMWPE are highlighted to demonstrate the reliability of the in vitro short-time testing method proposed. The complete experimental results were published in References 64,65.

Figure 7B shows an example of a MAT in the SBF (37°C) on UHMWPE. The maximum compressive stress σ_{max} as a controlled variable and as measured variables the maximum nominal compressive strain $\varepsilon_{c,max}$, nominal loss energy density $w_{c,L}$, and nominal strain energy density $w_{c,S}$ (both calculated through hysteresis) are plotted over the number of cycles N. The three measured variables show a step-like course with increasing σ_{max}, while the two hysteresis values take a constant (for $\sigma_{max} \leq 12.5$ MPa) or regressive course (for 12.5 MPa $< \sigma_{max} \leq 25$ MPa) within one stress step, $\varepsilon_{c,max}$ has a degressive course within every stress step. As the specimen fails at $\sigma_{max} = 27.5$ MPa, the three characteristic values increase drastically.

Figure 8A summarizes the CAT results on UHMWPE in air at RT and in SBF at 37°C. The maximum compressive stress σ_{max} of each CAT is plotted in semi-logarithmic application over the number of cycles to failure N_f. Significant differences between the two testing conditions are evident. For $\sigma_{max} = 25$ MPa, there is a difference in the number of cycles to failure of $N_{f,RT} = 529{,}531$ to $N_{f,SBF} = 183{,}434$. Furthermore, for $\sigma_{max} = 20$ MPa in air, a run-out is listed, whereas in SBF a run-out is achieved for $\sigma_{max} = 15$ MPa.

Figure 8B summarizes the results of the hardness measurements after CAT (Figure 8A). The percentage change in Martens hardness ΔHM_{CAT} in relation to the initial value HM_0 is plotted over the different testing conditions, with each hardness value averaged from three measurements. Dependencies can be seen for both the different maximum compressive stresses σ_{max} and the varying environmental conditions. For $\sigma_{max} = 30$ MPa the Martens hardness decreases to 71% of the initial value. In comparison to the tests in the SBF, differences of 8.4% for $\sigma_{max} = 25$ MPa (RT 94.3%; SBF 85.9%) and 6.6% for $\sigma_{max} = 20$ MPa (RT: 95.6%; SBF: 89.0%) can be seen.

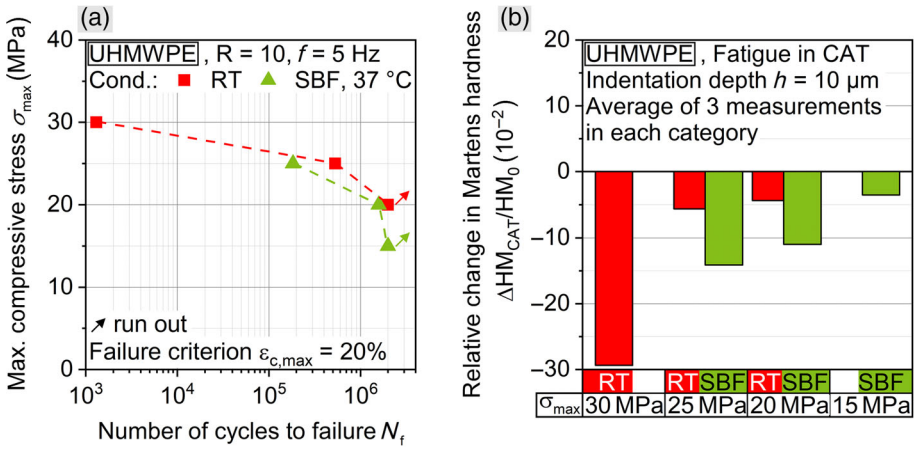

FIGURE 8 Exemplary results of (A) constant amplitude tests (CAT) in the form of trend S–N curves and (B) of the change in Martens hardness ΔHM_{CAT} after mechanical loading in the CAT in relation to the initial hardness HM_0 of UHMWPE.[65] UHMWPE, ultra-high molecular weight polyethylene

Figure 9 gives an overview of the FTIR spectroscopy scans before and after CAT. The normalized absorbance A (arbitrary unit) is plotted over the wavenumber $\tilde{\nu}$. The scaling of the wavenumber allows the consideration of all areas relevant for UHMWPE. In all subdiagrams (i.c. and after CAT), the characteristic absorptions at 2915 cm^{-1} (ν_a, asymmetric) and 2847 cm^{-1} (ν_s, symmetric) are caused by stretching of the methylene groups (—C—H_2—), at 1472 and 1463 cm^{-1} by bending of the methylene and at 1369 cm^{-1} by the methyl groups (—C—H_3). Furthermore, the peak at 2022 cm^{-1} is characteristic for twisting and at 730 cm^{-1} as well as 719 cm^{-1} for the rocking of the methyl groups.[66–69] Other absorptions are visible at 1576 and 1540 cm^{-1}, at 1740 cm^{-1}, and a broader activity in the range of 970–770 cm^{-1}.

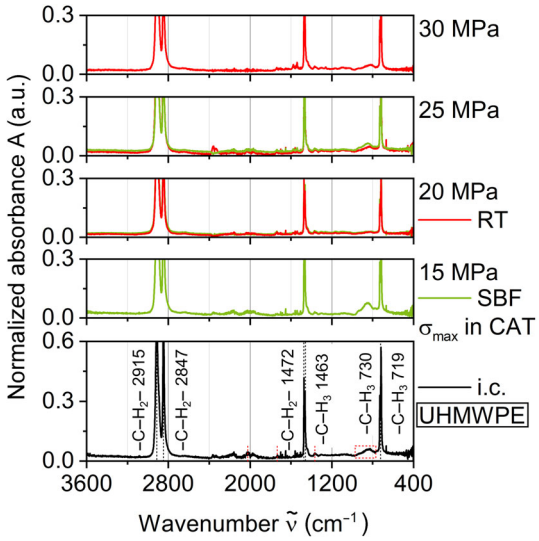

FIGURE 9 Exemplary results of Fourier-transform infrared spectroscopy on UHMWPE in initial condition (i.c.) and for the scans after mechanical loading in a constant amplitude test (CAT). The absorptions entered in the diagram are marked in black, all others in red. UHMWPE, ultra-high molecular weight polyethylene

4 | DISCUSSION

4.1 | Magnesium implants

The differences in corrosion behavior can be attributed to the porosity (Figure 2) and the slightly smaller grain size of Batch B (Table 1). Due to the small grain size, a continuous network of alloying elements forms over the entire sample, allowing it to act as a corrosion barrier. This phenomenon can be observed for magnesium alloys with the addition of RE elements. Furthermore, the addition of these elements increases the grain refinement, thus, mutually reinforcing both effects.[70,71] Based on the micro-, macrostructural, and corrosion investigations, Batches A and B were selected for the fatigue investigations, as the greatest differences were assumed. As suspected, the two selected batches show differences in fatigue behavior. These differences can mainly be attributed to the pore/defect density, which, according to Figure 2A, is higher for Batch A. In this context, the large, elongated pores (cf. Figure 2B, high equivalent pore diameter d_p and low sphericity S) for Batch A are particularly worth mentioning.

For the tests in the SBF, differences to the tests in air are already evident in the LCF range. Despite a shortened test duration and consequently a shortened exposure time to the SBF in this range, the number of cycles to failure is lower, although this decrease cannot be exclusively justified by the corrosive influence due to very short test durations of a few minutes. However, differences between the two batches are also apparent, but these are insignificant and require statistical verification. Thus, it is hypothesized that the influence of corrosion is dominant, as the differences in corrosion fatigue properties between the two batches are small despite different porosity and corrosion properties. Due to the increased surface roughness of the additively manufactured specimens and the corrosion scars, multiple crack initiation is present, so that the dominant damage mechanism cannot be determined without further effort. It should be noted, however, that the tests were carried out at constant technical stress, implying that the reduction in cross-section due to the degradation is not taken into account.

Below σ_{max} = 25 MPa, it was not possible to perform reproducible tests due to the calibration of the servo-hydraulic testing system used. Thus, it was not possible to achieve the defined maximum number of cycles N_{limit}. Nevertheless, a statement regarding the corrosion fatigue strength of the additively manufactured magnesium specimens can be made based on the study by Taylor.[72] For human long bones, the number of cycles to failure of $N_f = 10^5$ was achieved for cyclic

stresses of 23–30 MPa, so that the results for 25 MPa ($N_{f,A,SBF}$ = 527,390 and $N_{f,B,SBF}$ = 691,729), achieved in this study, are sufficient. A comparison with current literature is difficult since there are only a few studies on the corrosion fatigue behavior of magnesium in SBF. The few studies that do exist use different test conditions or different alloys. The authors are not aware of any studies on additively manufactured magnesium with these testing conditions. Studies investigating the influence of pre-corrosion on fatigue properties are not comparable due to different damage mechanisms.[51] Other studies used a stress ratio of $R = -1$ (fully-reversed loading) and a test frequency of $f = 10$ Hz in which a strong decrease in fatigue strength and a change in crack initiation from structural defects to corrosion scars were also observed.[45–47]

4.2 | Magnesium stents

The results of the fatigue and corrosion fatigue tests (Figure 4B) of the magnesium stents are to be interpreted in a similar way as in Section 4.1. Even for low numbers of cycles and thus for short test durations, significant differences to the reference tests in air become apparent due to the corrosive loading. With increasing test time in the HCF range, the fatigue properties decrease drastically, indicating a dominant corrosive influence. Due to the calibration of the testing system, it was not possible to test at lower maximum stresses than $\sigma_{max} < 25$ MPa and thus to achieve the defined maximum number of cycles $N_{limit} = 10^7$. A comparison with the current literature is not possible due to the lack of comparable studies.

4.3 | Titanium abutments

In contrast to the magnesium implants and stents, the titanium abutments used the principle of a MAT. Based on these results the load steps of the CAT were designed. When considering the maximum displacement (Figure 5) at the end of the respective load steps, a linear relationship results. For Grade 4 the displacement leaves this relationship at $F_{max} = 1.6$ kN and for Grade 5 at $F_{max} = 2$ kN (green bars), assuming damage initiation at these load steps and using these values for the following CAT. Based on the results of the CAT (Figure 6) it can be concluded that despite the good corrosion resistance of titanium alloys,[73] that definitely there is a corrosion influence on the fatigue properties. These findings can be made for the anterior and cheek tooth geometry, confirming the findings from MAT. The differences between the two alloys are due to the strength-increasing effect of the alloying elements and consistent with the literature.[73] Furthermore, significant differences between the two tooth geometries are recognizable, which can be explained by differences in cross-section and, consequently, by different applied stresses.

4.4 | UHMWPE implants

For UHMWPE, the MAT is evaluated as described in Section 4.3. If the maximum values at the beginning of each stress step are considered (Figure 7B), a linear relationship results. This correlation no longer applies to the three characteristic values from the fourth stress step $\sigma_{max} = 15$ MPa (green bar) onwards, so that damage initiation is expected and this maximum compressive stress is used to design the following CAT. The differences in fatigue behavior (Figure 8A) between the tests in SBF at 37°C and the reference tests in air at RT can be explained by the temperature-dependent properties of semi-crystalline thermoplastics. At higher temperatures, the mobility of the macromolecules increases whereas the resistance to mechanical deformation consequently decreases. According to Pampillo and Davis[74] and Kurtz et al.,[10] the properties of UHMWPE are in a linear relationship for temperatures between 0 and 60°C and decrease with increasing temperature. A correlation of the fatigue results with corresponding literature is difficult due to different experimental procedures and parameters. In the rarest of cases, testing was carried out in a body-like fluid. Comparable studies, which used at least a fluid, tested either under different stress ratios R, with different numbers of cycles to failure N_f or with different failure criteria. For example, Sobieraj et al. used $N_f = 250{,}000$ and $R = 0.04–0.05$ and Urriés et al. used 12% yield strain as failure criterion and $R = 0$. Within these two studies, fatigue strengths of $\Delta\sigma = 20.34$ and 22.70 MPa,[20] as well as 20 MPa,[22] were determined. The correlations of the hardness values (Figure 8B) after mechanical loading in CAT can be explained by the semi-crystalline structure of UHMWPE.[10] For lower stresses (HCF) mainly the amorphous phase is deformed, whereas at higher stresses (LCF) both phases (i.e., also the crystalline) are deformed.[78,79] As the mobility of the amorphous phase in particular increases with rising temperature, the resistance to mechanical stress decreases.[75]

For the results of the FTIR spectroscopy measurements, the smaller absorptions at 1576 and 1540 cm^{-1} are probably due to contamination and at 1740 cm^{-1} due to ester structures.[66,67,76] The broad activity in the range of 970–770 cm^{-1} probably characterizes the presence of a vinyl double bond (bending of C—H) occurring during the rupture of the macromolecules so that the latter two peaks represent oxidative (ester) and mechanical (vinyl) damage to the microstructure.[10,67,76,77] Based on the spectra, no correlation can be observed between increasing mechanical stress or exposure of the medium with the variation of the absorptions. Thus, the loss in mechanical stability is dominantly attributed to the influence of temperature.[10,76]

5 | CONCLUSIONS

The results of novel adaptable short-time in vitro testing procedures performed on four different implants allow several conclusions. A basic test rig was developed, which can be adapted according to the material class, implant geometry, and loading type to suit the particular application conditions. The results of all test procedures show that fatigue tests in air are not sufficient to characterize the application-relevant fatigue properties of implant materials, since the superposition of SBF was accompanied by a drastic decrease in fatigue properties, regardless of whether the implant is bioresorbable or permanent. In situ and ex

situ measuring equipment was used, which was adapted to the circumstances of the respective material to obtain a holistic understanding of the present damage mechanisms.

It was highlighted that the presented short-time testing method could be used to successfully estimate the fatigue strength of UHMWPE and titanium abutments while at the same time reducing the number of CAT, which were typically necessary to determine the fatigue strength of additively manufactured magnesium samples (standardized geometry) and the magnesium stents.

By means of the developed in vitro short-time testing method, new implant systems, independent of material or geometry, can be tested in a time-efficient manner and thus unsuitable implants can be excluded before further clinical investigations. For additional qualification of the method, besides the statistical validation of the results, a further adjustment of the testing conditions to the in vivo environment is required, for example, by also being able to observe cellular processes.

Especially for bioresorbable materials, a longer loading period must be considered, so that the fatigue behavior can be evaluated with progressive degradation in the human body. For the long periods as well as the adapted environmental conditions, the development of integrable bioreactors is necessary to assure sterility in a mechanical test set-up. For permanent implants and the corresponding field of application, the investigation of very high cycle numbers, which reflect a service life of several years, also plays a central role. Therefore, the fatigue properties with and without corrosive loading in the very HCF (VHCF) range are to be investigated in detail in the future.

ACKNOWLEDGEMENTS

The authors thank the German Research Foundation (Deutsche Forschungsgemeinschaft, DFG) for its financial support within the research project "Development and validation of an in vitro short-time testing method for the prediction of the in vivo behavior of absorbable metallic implant materials" (SM 214/4-1, WA 1672/40-1). The authors further thank the Materials and Process Department of Laser Zentrum Hannover e.V. (Hannover, Germany) for the provision of additively manufactured magnesium material, the Helmholtz-Zentrum Geesthacht (Geesthacht, Germany) for the provision of magnesium stents, Thomas Voigt Dentaltechnik GmbH (Hamburg, Germany) for the provision of titanium abutments and the Institute of New Materials and Nanotechnologies of National University of Science and Technology MISIS (Moscow, Russia) for the provision of UHMWPE bulk material in the context of excellent scientific cooperation.

CONFLICT OF INTEREST

The authors declare no potential conflict of interest.

AUTHOR CONTRIBUTIONS

Nils Wegner, Martin Klein, and Daniel Kotzem performed the experiments. Nils Wegner prepared the figures. Nils Wegner, Ronja Scholz, and Marina Knyazeva wrote the manuscript. Frank Walther supervised the projects and reviewed the manuscript.

DATA AVAILABILITY STATEMENT

The data that support the findings of this study are available from the corresponding author upon reasonable request.

ORCID

Nils Wegner https://orcid.org/0000-0003-0513-6030
Ronja Scholz https://orcid.org/0000-0001-9872-977X
Daniel Kotzem https://orcid.org/0000-0001-7869-2340
Marina Macias Barrientos https://orcid.org/0000-0002-6873-8277
Frank Walther https://orcid.org/0000-0003-2287-2099

REFERENCES

1. Glenske K, Donkiewicz P, Köwitsch A, et al. Applications for metals for bone regeneration. *Int J Mol Sci*. 2018;19(3):1-32.
2. Smeets R, Precht C, Hahn M, et al. Biocompatibility and osseointegration of titanium implants with a silver-doped polysiloxane coating: an in vivo pig model. *Int J Oral Maxillofac Implants*. 2017;32(6):1338-1345.
3. Witte F. The history of biodegradable magnesium implants: a review. *Acta Biomater*. 2010;6(5):1680-1692.
4. Triantafyllidis GK, Kazantzis AV, Karageorgiou KT. Premature fracture of a stainless steel 316L orthopaedic plate implant by alternative episodes of fatigue and cleavage decoherence. *Eng Failure Anal*. 2007;14(7):1346-1350.
5. Amel-Farzad H, Peivandi MT, Yusof-Sani SMR. In-body corrosion fatigue failure of a stainless steel orthopaedic implant with a rare collection of different damage mechanisms. *Eng Failure Anal*. 2007;14(7):1205-1217.
6. Singh Raman RK, Jafari S, Harandi SE. Corrosion fatigue fracture of magnesium alloys in bioimplant applications: a review. *Eng Fract Mech*. 2015;137:97-108.
7. Maksimkin AV, Senatov FS, Anisimova N, et al. Multilayer porous UHMWPE scaffolds for bone defects replacement. *Mater Sci Eng C*. 2017;73:366-372.
8. Senatov FS, Kopylov AN, Anisimova N, Kiselevsky MV, Maksimkin AV. UHMWPE-based nanocomposite as a material for damaged cartilage replacement. *Mater Sci Eng C*. 2015;48:566-571.
9. Senatov FS, Gorshenkov MV, Tcherdyntsev VV, et al. Biocompatible polymer composites based on ultrahigh molecular weight polyethylene perspective for cartilage defects replacement. *J Alloys Compd*. 2014;586:544-547.
10. Kurtz S, ed. *UHMWPE Biomaterials Handbook – Ultra-high Molecular Weight Polyethylene in Total Joint Replacement and Medical Devices*. 3rd ed. Amsterdam: Elsevier Inc.; 2016.
11. Brach Del Prever EM, Bistolfi A, Bracco P, Costa l. UHMWPE for arthroplasty - past or future? *J Orthop Traumatol*. 2009;10(1):1-8.
12. Senatov FS, Niaza KV, Salimon AI, Maksimkin AV, Kaloshkin SD. Architected UHMWPE simulating trabecular bone tissue. *Mater Today Commun*. 2018;14:124-127.
13. Braun S, Sonntag R, Schroeder S, et al. Backside wear in acetabular hip joint replacement. *Acta Biomater*. 2019;83:467-476.
14. Cowie RM, Briscoe A, Fisher J, Jennings LM. Wear and friction of UHMWPE-on-PEEK OPTIMA. *J Mech Behav Biomed Mater*. 2019;89:65-71.
15. Abdelgaied A, Fisher J, Jennings LM. A comprehensive combined experimental and computational framework for pre-clinical wear simulation of total knee replacements. *J Mech Behav Biomed Mater*. 2018;78:282-291.
16. Zeman J, Ranusa M, Vrbka M, Gallo J, Krupka I, Hartl M. UHMWPE acetabular cup creep deformation during the run-in phase of THA's life cycle. *J Mech Behav Biomed Mater*. 2018;87:30-39.

17. Ansari F, Ries MD, Pruitt L. Effect of processing, sterilization and crosslinking on UHMWPE fatigue fracture and fatigue wear mechanisms in joint arthroplasty. *J Mech Behav Biomed Mater*. 2016;53:329-340.
18. Oral E, Malhi AS, Muratoglu OK. Mechanisms of decrease in fatigue crack propagation resistance in irradiated and melted UHMWPE. *Biomaterials*. 2006;27:917-925.
19. Oral E, Ghali BW, Rowll SL, Micheli BR, Lozynsky AJ, Muratoglu OK. A surface crosslinked UHMWPE stabilized by vitamin E with low wear and high fatigue strength. *Biomaterials*. 2010;31:7051-7060.
20. Sobieraj MC, Murphy J, Brinkman J, Kurtz S, Rimnac C. Monotonic and fatigue behavior of five clinically relevant conventional and highly crosslinked UHMWPEs in the presence of stress concentrations. *J Mech Behav Biomed Mater*. 2013;28:244-253.
21. Medel FJ, Peña P, Cegoñino J, Gómez-Barrena E, Puértolas JA. Comparative fatigue behavior and toughness of remelted and annealed highly crosslinked polyethylenes. *J Biomed Mater Res B Appl Biomater*. 2007;83:380-390.
22. Urriés I, Medel FJ, Rios R, Gómez-Barrena E, Puértolas J. Comparative cyclic stress-strain and fatigue resistance behavior of electron-beam- and gammairradiated ultrahigh molecular weight polyethylene. *J Biomed Mater Res*. 2004;70B:152-160.
23. Ries MD, Weaver K, Rose RM, Gunther J, Sauer W, Beals N. Fatigue strength of polyethylene after sterilization by gamma irradiation or ethylene oxide. *Clin Orthop Relat Res*. 1996;333:87-95.
24. Weightman B, Light D. A comparison of RCH 1000 hi-fax 1900 ultra-high molecular weight polyethylenes. *Biomaterials*. 1985;6:177-183.
25. Hung H-C, Huang C-S, Pan Y-H. The compressive strength of implant-abutment complex with different connection designs. *J Dent Sci*. 2019;14:318-324.
26. Murr LE, Gaytan SM, Medina F, et al. Characterization of Ti–6Al–4V open cellular foams fabricated by additive manufacturing using electron beam melting. *Mater Sci Eng A*. 2010;527:1861-1868.
27. Dallago M, Fontanari V, Torresani E, et al. Fatigue and biological properties of Ti-6Al-4V ELI cellular structures with variously arranged cubic cells made by selective laser melting. *J Mech Behav Biomed Mater*. 2018;78:381-394.
28. Singh R, Lee P, Dashwood RJ, Lindley TC. Titanium foams for biomedical applications: a review. *Mater Technol*. 2010;25:127-136.
29. Sivaraman K, Chopra A, Narayan AI, Balakrishnan D. Is zirconia a viable alternative to titanium for oral implant? A critical review. *J Prosthodont Res*. 2018;62:121-133.
30. Coray R, Zeltner M, Özcan M. Fracture strength of implant abutments after fatigue testing: a systematic review and meta-analysis. *J Mech Behav Biomed Mater*. 2016;62:333-346.
31. Blum K, Wiest W, Fella C, et al. Fatigue induced changes in conical implant-abutment connections. *Dent Mater*. 2015;31:1415-1426.
32. Gratton DG, Aquilino SA, Stanford CM. Micromotion and dynamic fatigu properties of the dental implant-abutment interface. *J Prosthet Dent*. 2001;85(1):47-52.
33. Tsumita M, Kokubo Y, Kano T, Sasaki K. The effect of fatigue loading on the screw joint stability of zirconium abutment. *J Prosthodont*. 2013;57:219-223.
34. Cosola S, Toti P, Babetto E, Covani U, Peñarrocha-Diago M, Peñarrocha-Oltra D. In-vitro fatigue and fracture performance of three different ferrulized implant connections used in fixed prosthesis. *J Dent Sci*. 2021;16:397-403.
35. Foong JK, Judge RB, Palamara JE, Swain MV. Fracture resistance of titanium and zirconia abutments: an in vitro study. *J Prosthet Dent*. 2013;109(5):304-312.
36. Freitas-Júnior AC, Rocha EP, Bonfante EA, et al. Biomechanical evaluation of internal and external hexagon platform switched implant-abutment connections: an in vitro laboratory and three-dimensional finite element analysis. *Dent Mater*. 2012;28:e218-e228.
37. Staiger MP, Pietak AM, Huadmai J, Dias G. Magnesium and its alloys as orthopedic biomaterials: a review. *Biomaterials*. 2006;27(9):1728-1734.
38. Farraro KF, Kim KE, Woo SL, Flowers JR, McCullough MB. Revolutionizing orthopaedic biomaterials: the potential of biodegradable and bioresorbable magnesium-based materials for functional tissue engineering. *J Biomech*. 2014;47(9):1979-1986.
39. Jung O, Smeets R, Porchetta D, et al. Optimized in vitro procedure for assessing the cytocompatibility of magnesium-based biomaterials. *Acta Biomater*. 2015;23:354-363.
40. Jung O, Smeets R, Kopp A, et al. PEO-generated surfaces support attachment and growth of cells in vitro with no additional benefit for micro-roughness in Sa (0.2–4 μm). *In Vivo*. 2016;30:27-33.
41. Li Z, Gu X, Lou S, Zheng Y. The development of binary mg-Ca alloys for use as biodegradable materials within bone. *Biomaterials*. 2008;29:1329-1344.
42. Kannan MB, Raman RKS. In vitro degradation and mechanical integrity of calcium-containing magnesium alloys in modified-simulated body fluid. *Biomaterials*. 2008;29:2306-2314.
43. Ghazizadeh E, Jabbari AH, Sedighi M. In vitro corrosion-fatigue behavior of biodegradable mg/HA composite in simulated body fluid. *J Magnesium Alloys*. 2021;353-356.
44. Harandi SE, Singh Raman RK. Appropriate corrosion-fatigue testing of magnesium alloys for temporary bioimplant applications. In: Singh A, Solanki K, Manuel MV, Neelameggham NR (eds) *Magnesium Technology*; 2016;353–356.
45. Bian D, Zhou W, Liu Y, Li N, Zheng Y, Sun Z. Fatigue behaviors of HP-mg, mg-Ca and mg-Zn-Ca biodegradable metals in air and simulated body fluid. *Acta Biomater*. 2016;41:351-360.
46. Gu XN, Zhou WR, Zheng YF, et al. Corrosion fatigue behaviors of two biomedical mg alloys - AZ91D and WE43 - in simulated body fluid. *Acta Biomater*. 2010;6:4605-4613.
47. Jafari S, Raman RKS, Davies CHJ, Hofstetter J, Uggowitzer PJ, Löffler JF. Stress corrosion cracking and corrosion fatigue characterisation of MgZn1Ca0.3 (ZX10) in a simulated physiological environment. *J Mech Behav Biomed Mater*. 2017;65:634-643.
48. Jafari S, Singh Raman RK, Davies CHJ. Corrosion fatigue of a magnesium alloy in modified simulated body fluid. *Eng Fract Mech*. 2015;137:2-11.
49. Liu M, Wang J, Zhu S, et al. Corrosion fatigue of the extruded mg-Zn-Y-Nd alloy in simulated body fluid. *J Magnesium Alloys*. 2020;8:231-240.
50. Han L, Zhang Z, Dai J, et al. The influence of alternating cyclic dynamic loads with different low frequencies on the bio-corrosion behaviors of AZ31B magnesium alloy in vitro. *Bioact Mater*. 2021.7, 263–274.
51. Zhao J, Gao LL, Yuan Y, Chen X. Biodegradable behaviour and fatigue life of ZEK100 magnesium alloy in simulated physiological environment. *Fatigue Fract Eng Mater Struct*. 2015;38:904-913.
52. Ormiston JA. Bioabsorbable coronary stents. *Circ Cardiovasc Interv*. 2009;2:225-260.
53. Fischmann DL. A randomized comparison of coronary artery-stent placement and balloon angioplasty in the treatment of coronary artery disease. *N Engl J Med*. 1994;331:496-501.
54. Bowen PK. A new in vitro - in vivo correlation for bioabsorbable magnesium stents from mechanical behavior. *Mater Sci Eng C*. 2013;33:5064-5070.
55. Wang Q, Fang G, Zhao YH, Zhou J. Improvement of mechanical performance of bioresorbable magnesium alloy coronary artery stents through stent pattern redesign. *Appl Sci*. 2018;8:2461.
56. Gastaldi D, Sassi V, Petrini L, Vedani M, Trasatti S, Migliavacca F. Continuum damage model for bioresorbable magnesium alloy devices – application to coronary stents. *J Mech Behav Biomed Mater*. 2011;4:352-365.
57. Shen Z, Zhao M, Zhou X, et al. A numerical corrosion-fatigue model for biodegradable Mg alloy stents. *Acta Biomater*. 2019;97:671-680.
58. Cui X, Peng K, Liu S, et al. A computational modelling of the mechanical performance of a bioabsorbable stent undergoing cyclic loading. *Proc Struct Integr*. 2019;15:67-74.
59. Maier P, Griebel A, Jahn M, et al. Corrosion bending fatigue of RESOLOY and WE43 magnesium alloy wires. *Magnesium Technol*. 2019; 2019:175-181.
60. Griebel A, Schaffer J. Fatigue and corrosion fatigue of cold drawn WE43 wires. *Magnesium Technol*. 2015;2015:303-307.

61. Kokubo T, Kushitani H, Sakka S. Solutions able to reproduce in vivo surface-structure changes in bioactive glass-ceramic A-W^3. *J Biomed Mater Res*. 1990;24:721-734.
62. Wegner N, Kotzem D, Wessarges Y, et al. Corrosion and corrosion fatigue properties of additively manufactured magnesium alloy WE43 in comparison to titanium alloy Ti-6Al-4V in physiological environment. *Materials*. 2019;12(18):2892.
63. Wegner N, Kotzem D, Walther F. Korrosions- und Korrosionsermüdungsverhalten der additiv gefertigten Magnesiumlegierung WE43 für biomedizinische Anwendungen. Werkstoffprüfung 2019 – Fortschritte in der Werkstoffprüfung für Forschung Und Praxis, Hrsg.: H.-J. Christ, 2019. pp. 161–166.
64. Scholz R, Knyazeva M, Porchetta D, et al. Development of biomimetic in vitro fatigue assessment for UHMWPE implant materials. *J Mech Behav Biomed Mater*. 2018;85:94-101.
65. Wegner N, Scholz R, Knyazeva M, Walther F. Service life characterization of orthopedic implant material made of ultra-high molecular weight polyethylene under physiological conditions. *J Mech Behav Biomed Mater*. 2020;104:103617.
66. Costa L, Bracco P, Brach del Prever E, Luda MP, Trossarelli L. Analysis of products diffused into UHMWPE prosthetic components in vivo. *Biomaterials*. 2001;22:307-315.
67. Workman J. *Handbook of organic compounds: NIR, IR, Raman, and UV spectra featuring polymers and surfaces*. Cambridge, MA: Academic Press; 2001.
68. Kuptsov AH, Zhizhin GN. *Handbook of Fourier transform Raman and infrared spectra of polymers*. Amsterdam: Elsevier; 1998.
69. Solit A, Hummel DO, Simak P. Computer-supported infrared spectroscopy ofpolyethylene, ethylene copolymers, and amorphous poly(alkyl)ethylenes. *Macromol Symp*. 1986;5:105-133.
70. Qin Y, Wen P, Guo H, et al. Additive manufacturing of biodegradable metals: current research status and future perspectives. *Acta Biomater*. 2019;98:3-22.
71. Soderlind J, Cihova M, Schäublin R, Risbud S, Löffler JF. Towards refining microstructures of biodegradable magnesium alloy WE43 by spark plasma sintering. *Acta Biomater*. 2019;98:67-80.
72. Taylor D. Fatigue of bone and bones: an analysis based on stressed volume. *J Orthop Res*. 1998;16:163-169.
73. Geetha M, Singh AK, Asokamani R, Gogia AK. Ti based biomaterials, the ultimate choice for orthopaedic implants – a review. *Prog Mater Sci*. 2009;54:397-425.
74. Pampillo CA, Davis LA. Temperature dependence of the yield and flow stresses of linear high-molecular-weight polyethylene. *J Appl Phys*. 1972;43:4277-4285.
75. Gilbert JL, Merkhan I. Rate effects on the microindentation-based mechanical properties of oxidized, crosslinked, and highly crystalline ultrahigh-molecularweight polyethylene. *J Biomed Mater Res*. 2004;71:549-558.
76. Rocha M, Mansur A, Mansur H. Characterization and accelerated ageing of UHMWPE used in orthopedic prosthesis by peroxide. *Materials*. 2009;2:562-576.
77. Senatov FS, Baranov AA, Muratov DS, Gorshenkov MV, Kaloshkin SD, Tcherdyntsev VV. Microstructure and properties of composite materials based on UHMWPE after mechanical activation. *J Alloy Comp*. 2014;615:573-577.
78. Butler MF, Donald AM, Ryan AJ. Time resolved simultaneous small- and wide-angle X-ray scattering during polyethylene deformation – II. Cold drawing of linear polyethylene. *Polymer*. 1997;39:39-52.
79. Bathias C, Pineau A. *Fatigue of Materials and Structures: Fundamentals*. Hoboken, NJ: John Wiley & Sons; 2010.

How to cite this article: Wegner N, Klein M, Scholz R, Kotzem D, Macias Barrientos M, Walther F. Mechanical in vitro fatigue testing of implant materials and components using advanced characterization techniques. *J Biomed Mater Res*. 2022;110(4):898-909. doi:10.1002/jbm.b.34970